Deep Resources Engineering 1 (2024) 100114

Contents lists available at ScienceDirect

Deep Resources Engineering

journal homepage: www.keaipublishing.com/en/journals/deepre/

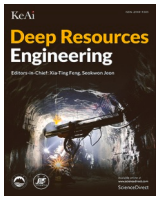

Full Length Article

Study on the time delay failure characteristics of sandstone unloading under dynamic disturbance

Huafeng Deng [a,*], Yening Huang [a], Yao Xiao [a], Pengfei Xu [a], Jianlin Li [a], Mingyang Wang [b]

[a] Key Laboratory of Geological Hazards on Three Gorges Reservoir Area, Ministry of Education, China Three Gorges University, Yichang, Hubei 443002, China
[b] State Key Laboratory of Disaster Prevention and Mitigation of Explosion and Impact, Army Engineering University of PLA, Nanjing, Jiangsu 210007, China

ARTICLE INFO

Keywords:
Time delay
Unloading
Deformation characteristics
Destructive form
Particle Flow Program

ABSTRACT

The rockburst caused by underground engineering excavation exhibits a significant lag effect. Studies have shown that the occurrence of lag-type rockburst is closely related to the delayed failure of rocks. This paper focuses on the delayed failure characteristics of unloading-damaged sandstone under the combined action of static load and dynamic disturbance. Numerical simulations are utilized to analyze the delayed failure evolution characteristics and failure mechanisms of sandstone. The results indicate that in triaxial unloading delay failure tests, the duration of loading decreases exponentially with the increase of initial unloading damage. Compared to static load conditions, the duration of loading under dynamic disturbance decreases by more than 43 %, and the average strain rate significantly increases. The number of cracks at the endpoint of triaxial unloading delay failure increases as initial unloading damage decreases, with a substantial increase in the number of cracks under dynamic disturbance. These findings provide a valuable reference for the timeliness and delayed rockburst analysis and interpretation of rock damage and failure under high-stress levels.

1. Introduction

Rockburst is a common engineering disaster encountered during the excavation of underground rock mass engineering [1,21,37,55]. It can be classified into immediate rockburst [13,14,20] and time-delayed rockburst [4,12] based on the timing of its occurrence. Statistical results show that most rock bursts occur within minutes to hours or even longer after excavation [46], such as the diversion tunnel of the Minjiang Taipingyi Hydropower Station [54], the Lujialing Tunnel in Chongqing [26], the diversion tunnel of the Jinping II Hydropower Station [24,51], and the Qinling Railway Tunnel [21]. Time delayed rockburst occurs after a period of rock excavation, which has a greater impact on engineering safety and poses a severe challenge to the safety of underground engineering construction. Time-delayed rockburst occurs after a period of rock excavation, posing a significant threat to engineering safety and presenting severe challenges to the safety of underground construction. Consequently, the mechanism of delayed rockburst has garnered considerable attention from scholars, leading to numerous experiments and theoretical studies.

Many scholars have conducted extensive theoretical and experimental research on the mechanism of delayed rockburst in rock masses. Feng et al., [15] employed a combination of indoor experiments, numerical simulations, and on-site monitoring techniques to study rockburst, concluding that delayed rockburst is caused by external disturbances following stress adjustment and equilibrium after unloading from tunnel excavation. [17,18] conducted various harmonic wave impact rockburst tests, establishing the induced relationship between dynamic load, energy, and rockburst under sinusoidal waveform dynamic disturbance. Wang and Huang [41] analyzed actual cases of water diversion tunnel rockburst and found that rockburst occurred under the combined action of original rock stress and emitted tensile waves. Kang et al., [32] analyzed based on stability theory that rocks are in an unstable equilibrium state after possessing a large amount of strain energy. If disturbance interference is applied to the rock again, it will become unstable, and this was applied to the analysis of rock burst criteria. These studies systematically explain that original rock stress and external dynamic disturbance are two critical mechanisms influencing rockburst occurrence, as demonstrated through comparisons of on-site rockburst cases.

The delayed occurrence of rockburst is closely related to the delayed failure of rocks. Therefore, numerous scholars have investigated different stress paths and conducted delayed failure tests on various rock

* Corresponding author.
E-mail address: dhf8010@ctgu.edu.cn (H. Deng).

https://doi.org/10.1016/j.deepre.2024.100114
Received 28 August 2024; Received in revised form 24 September 2024; Accepted 25 September 2024
Available online 4 October 2024

types under static and dynamic disturbances. For instance, Su et al., [39] performed joint tests involving low-frequency periodic disturbance loads and high-stress static loads on granite to simulate the rockburst process. Their results indicated that low-frequency periodic disturbance loads propagated over greater distances and carried higher energy, thus facilitating deformation and failure of high-stress surrounding rock. Ma et al., [33] observed that the degree of layered fracturing of roadway surrounding rock varied under different combinations of dynamic and static loads, with increasing combined stress exacerbating the fracturing. Li et al., [27] conducted dynamic and static combination experiments under two stress paths: static stress combined with loading disturbance, and static stress combined with unloading disturbance. They proposed a rockburst dynamic criterion based on the dynamic and static energy index. Wang et al., [43] utilized an improved Hopkinson bar (SHSP) test system to observe trends in dynamic deformation modulus, rebound strain, and dynamic peak stress with respect to the number of impact disturbances. Ye et al., [50] conducted two dynamic and static combination tests on fine sandstone using an improved SHPB experimental system, namely "constant confining pressure to axial pressure" and "constant axial pressure to confining pressure." They compared and analyzed the dynamic and static combination strength, elastic modulus, and average strain rate changes of the two stress paths, revealing different trends. These findings suggest that rocks exhibit significant differences in deformation characteristics, strength parameters, failure characteristics, and energy release under static and dynamic disturbances.

The aforementioned studies underscore the critical impact of original rock stress and external dynamic disturbances on the delayed failure of rock masses. Excavation unloading disrupts the mechanical balance of the original rock, placing the rock mass in a high strain energy state and causing varying degrees of unloading damage to the surrounding rock. Additionally, excavation and unloading damage to the rock mass can be influenced by blasting vibrations during nearby construction, leading to dynamic disturbances from different temporal and spatial positions. However, previous studies on time-delayed failure have rarely considered the influence of initial unloading damage. Therefore, this article aims to investigate the delayed failure characteristics of sandstone under static and dynamic disturbances, accounting for different initial unloading damages. Through numerical simulation of the entire experimental process, the delayed failure evolution characteristics and failure mechanisms of sandstone are analyzed.

2. Experimental scheme design

2.1. Sample preparation

Sandstone is widely distributed on the surface [52,53]. It is a common type of rock in engineering construction projects such as slopes, mining, high-speed rail construction, dams, and underground tunnels [16,23,29,44]. Due to its strong representativeness, the experiment focused on sandstone as the research object. The rock sample used is porous calcium cemented sericite medium grained quartz sandstone, which is slightly weathered and has a particle size of approximately 0.3–0.5 mm [8]. Strictly following the specifications [34], the standard cylindrical rock sample with a diameter of 50 mm and a height of 100 mm was processed. The sample is then rigorously screened based on wave velocity and density, as detailed in studies by [7,9]. The typical rock sample selected is shown in Fig. 1. Among them, the density of the rock sample is 2.60 g/m^3. The average wave velocity of the rock sample is 2500 m/s, and rock samples with concentrated wave velocity and density are selected for the experiment.

2.2. Three axis unloading delay failure test plan

Underground engineering rock masses are generally under triaxial stress before excavation. Deformation and failure after excavation

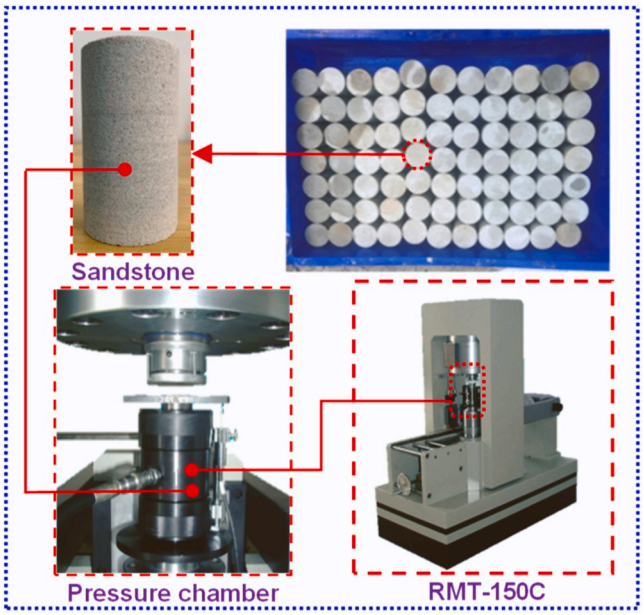

Fig. 1. Photos of typical rock samples and test equipment.

typically occur in the surrounding rock at a certain depth near the tunnel wall. Due to the unloading effect of excavation, the rock mass in this area is approximately in a one-dimensional, two-dimensional, or three-dimensional stress state and is also affected by external dynamic disturbances (such as blasting and excavation vibrations in critical areas). Considering this stress characteristic, the underground engineering rock mass is mainly affected by the combined action of geostress and dynamic disturbances. Its environment is shown in Fig. 2(a), and its stress state can be simplified as shown in Fig. 2(b) [50].

The rock mass at location A is mainly subjected to the combined effects of triaxial static loads and vertical dynamic disturbances. Therefore, the rock mass at location A can be considered for the unloading effect of confining pressure, and static and dynamic load tests under triaxial unloading conditions can be conducted for simulation.

Triaxial compression tests were conducted on rock samples under a confining pressure of 20 MPa to obtain the peak triaxial compression strength. In order to accurately simulate the stress state of actual engineering projects such as tunnel excavation and facilitate control, considering the unloading path of constant axial pressure unloading confining pressure [38], triaxial unloading tests were conducted under the same confining pressure to obtain the failure confining pressure of triaxial unloading.

In the static and dynamic disturbance action under unloading delay

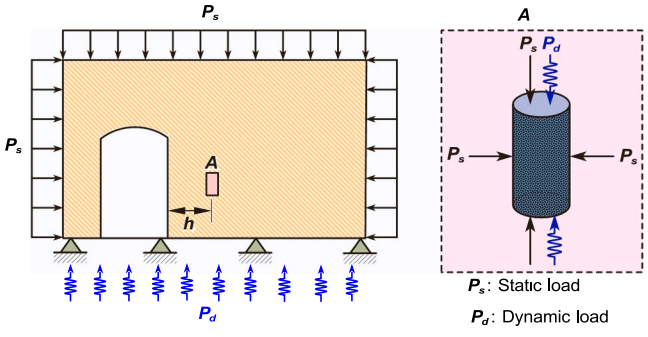

Fig. 2. Schematic diagram of rock mass stress in underground engineering [50].

failure test, the influence of initial unloading damage is primarily considered. Referring to the definition of initial unloading damage in the literature [10], as shown in Eq. (1), six types of initial unloading damage are mainly considered: 95 %, 90 %, 85 %, 80 %, 75 %, and 70 %.

$$X_\sigma = \frac{\left(\sigma_3^0 - \sigma_3^i\right)}{\left(\sigma_3^0 - \sigma_3^f\right)} \times 100\% \tag{1}$$

Where: X_σ represents the initial unloading damage, σ_3^0 is the confining pressure value before unloading, σ_3^i represents the confining pressure value at step i after unloading, and σ_3^f represents the confining pressure value at the time of failure in the triaxial unloading test.

The steps of the triaxial unloading delay failure test under static load are shown in Fig. 3. The first step is to load at a rate of 0.1 MPa/s to a static water pressure state, then maintain the confining pressure constant and continue to load the axial pressure at the same rate to the initial axial pressure (corresponding to 80 % of the peak strength of triaxial compression under confining pressure). This setting can meet the requirement of rock sample failure during unloading process [3,22]. The second step is to maintain the axial pressure constant and unload the confining pressure at a rate of 0.1 MPa/s to the specified initial unloading damage values (95 %, 90 %, 85 %, 80 %, 75 %, and 70 %), simulating different degrees of excavation unloading damage. Step three, when the confining pressure is unloaded to the specified confining pressure, keep the confining pressure and axial pressure constant until the specimen undergoes time-dependent failure.

In the triaxial unloading delay failure test under dynamic disturbance, the influence of disturbance load is further considered in the unloading delay stage based on the triaxial unloading delay failure test under static load. As shown in Fig. 4, during the third step of loading, maintain the confining pressure constant and apply axial dynamic disturbance. Referring to previous research experience [11,31,47], The dynamic disturbance form is selected as sine disturbance mode, with a disturbance frequency of 0.2 Hz and a disturbance amplitude of 10 kN, until the sample is destroyed.

3. Time delayed failure characteristics of sandstone under unloading damage under dynamic disturbance

3.1. Characteristics of stress-strain curve

The stress-strain curves of typical triaxial unloading delay failure tests under static and dynamic disturbance are shown in Figs. 5 and 6, with relevant deformation and duration of load statistics provided in Table 1.

Based on Figs. 5 and 6, and Table 1, the following conclusions can be drawn:

(1) Under static load and dynamic disturbance, the stress-strain curves of rock samples with varying initial unloading damages are generally consistent. All rock samples fail after a period of axial load, followed by a rapid decrease in the curves. Once reaching the residual stage, the strength stabilizes.

(2) During the time-delay stage, as the initial unloading damage increases, the axial strain increment under static load and dynamic disturbance gradually decreases. When the initial unloading damage increases from 70 % to 95 %, the axial strain increment under static load decreases from 2.28×10^{-3} to 0.84×10^{-3}, a reduction of approximately 63 %. Similarly, the axial strain increment under dynamic disturbance decreases from 3.28×10^{-3} to 0.88×10^{-3}, a reduction of about 73 %.

(3) Under the action of static load, all initial unloading damage rock samples fail after a certain period of axial loading, showing a significant time lag characteristic. Compared with the static load effect, the holding time of different initial unloading damages under dynamic disturbance is significantly reduced (Fig. 7), and the holding time of each initial unloading damage rock sample is reduced by more than 43 % on the basis of the corresponding static load effect. Comparison shows that under lower initial unloading damage, dynamic disturbance has a greater impact on the holding time of rock samples, with a larger difference between the two. However, under high initial unloading damage, dynamic disturbance has a smaller impact on the holding time of rock samples, with a smaller difference between the two.

3.2. Deformation law analysis

The axial strain-time curves of triaxial unloading delay failure tests under different unloading conditions for static loads and dynamic disturbances are shown in Fig. 8.

From Fig. 8, it can be observed that the strain-time curve of the unloading delay failure test under static load and dynamic disturbance resembles that of a creep test, with three stages: attenuation deformation stage, constant velocity deformation stage, and accelerated deformation stage. Additionally, the slope of the axial strain-time curve decreases with the reduction of initial unloading damage.

Due to varying initial unloading damages, significant differences exist in the delayed failure effects of rock samples. To quantitatively analyze the strain rate changes during the triaxial unloading delayed failure process, the corresponding load duration and strain increment during the constant velocity deformation stage under different initial unloading damages were statistically analyzed. The results are shown in Table 2, where the average strain rate during the constant velocity deformation stage of the triaxial unloading delay failure process is calculated by Eq. (2). Xu et al. [48]

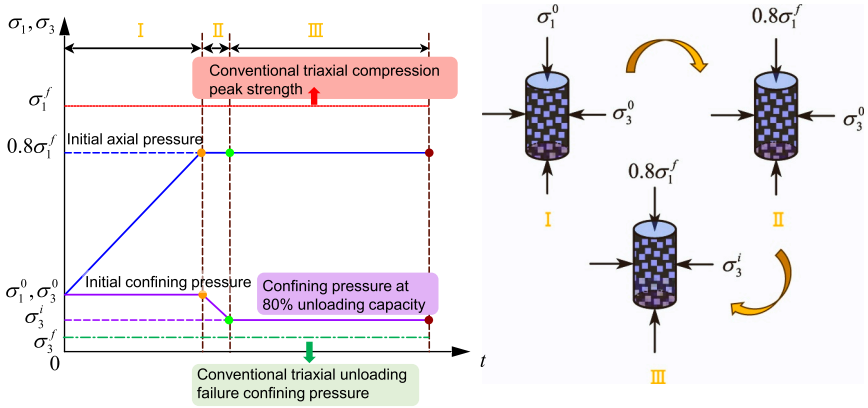

Fig. 3. Schematic diagram of three-axis unloading delay failure test under static load (taking 80 % initial unloading damage as an example).

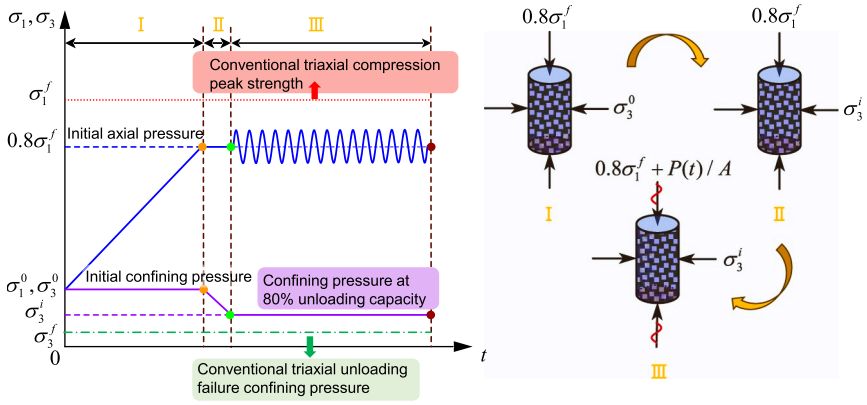

Fig. 4. Schematic diagram of three-axis unloading delay failure test under dynamic disturbance (taking 80 % initial unloading damage as an example).

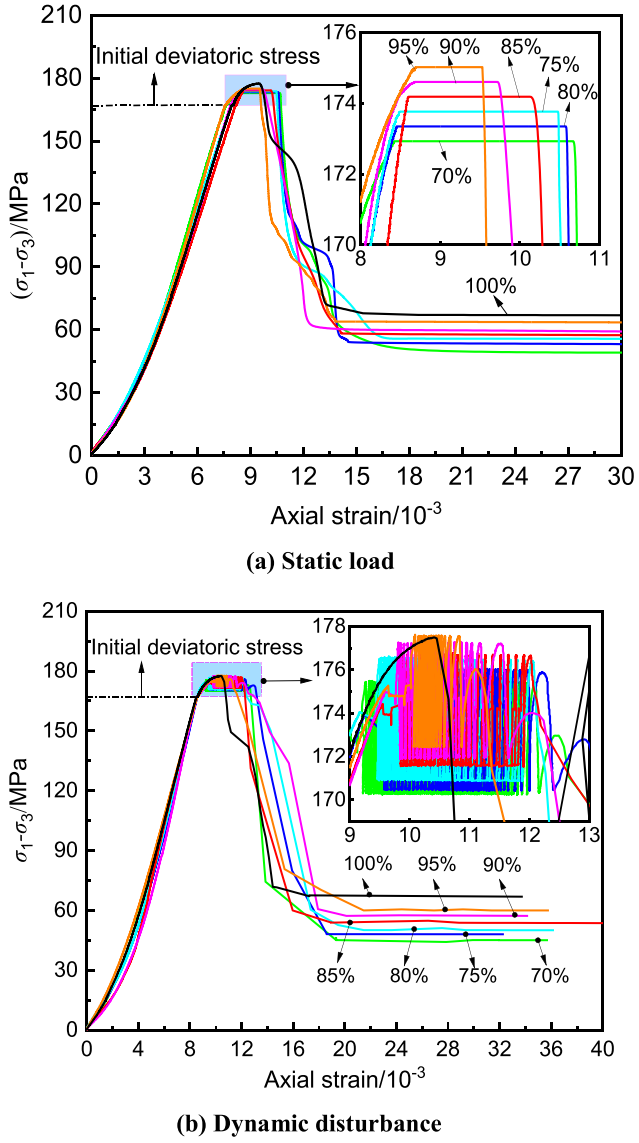

Fig. 5. Stress-strain curve.

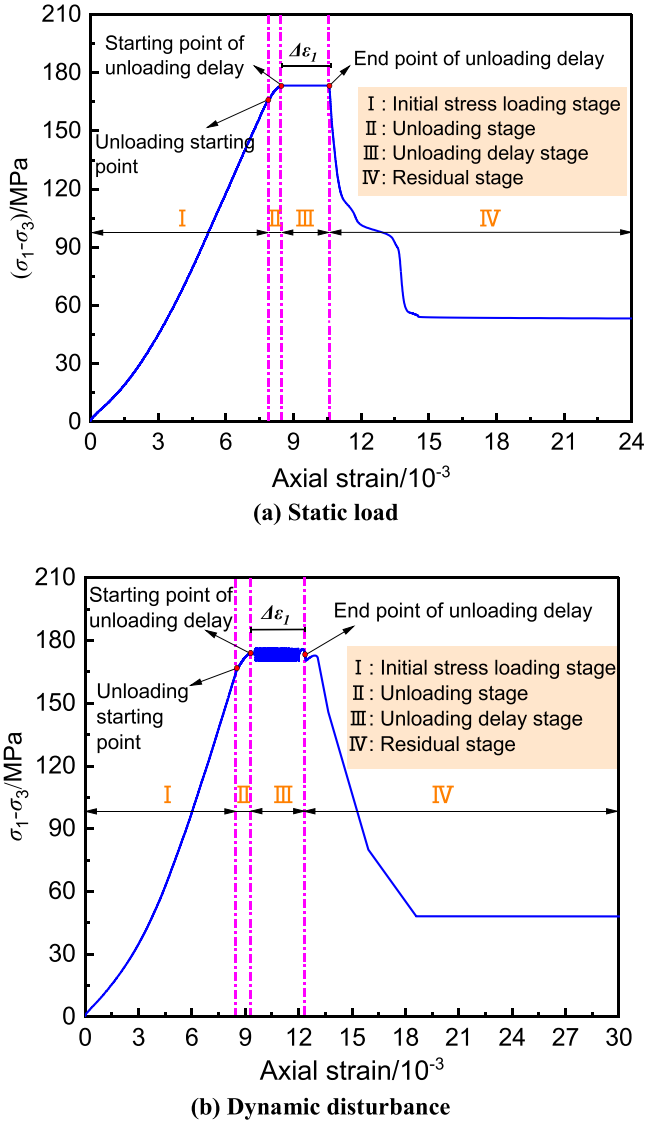

Fig. 6. Stress-strain curve (taking 75 % initial unloading damage as an example).

$$\overline{v}_{\varepsilon} = \frac{\left|\varepsilon_t^{end} - \varepsilon_t^{start}\right|}{\Delta t} \tag{2}$$

Where: $\overline{v}_{\varepsilon}$ is the average strain rate; ε_t^{end} is the end strain value of the constant velocity deformation stage in the unloading delay stage; ε_t^{start} is the initial strain value of the constant velocity deformation stage in the unloading delay stage; Δt is the total duration of the constant velocity deformation stage in the unloading delay stage. The average strain rate

Table 1
Results of three-axis unloading delay failure test.

Initial unloading damageX_σ/%	Strain increment $\Delta\varepsilon_1/10^{-3}$		Duration of load t_f/min	
	Static load	dynamic disturbance	Static load	dynamic disturbance
70	2.28	3.28	106.30	58.23
75	2.14	3.17	72.22	36.37
80	1.98	1.47	49.31	25.14
85	1.65	1.12	29.11	14.62
90	1.14	0.99	14.32	7.23
95	0.84	0.88	4.63	2.63
100	/	/	0.10	0.10

Note: Strain increment refers to the strain between the starting and ending points of the time delay (as shown in Fig. 6); The duration of the load is the duration between the starting and ending points of the time delay.

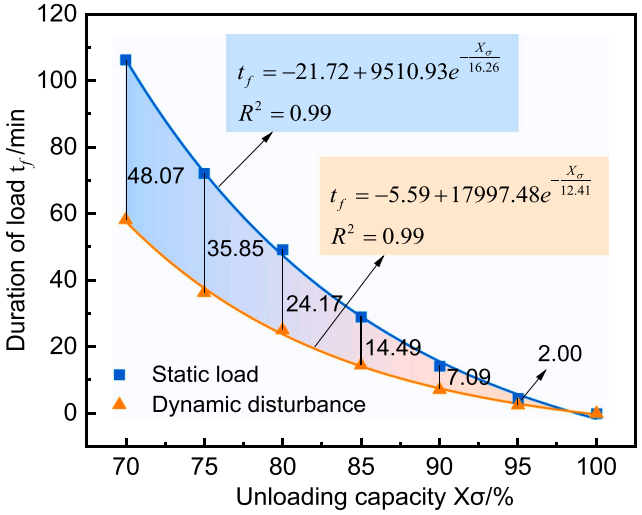

Fig. 7. Load duration-initial unloading damage curve.

calculated according to Eq. (2) is shown in Fig. 9.

To reflect the irreversible deformation trend of the unloading delay stage under dynamic disturbance, the relative deformation coefficient (R) is introduced for statistical analysis, as defined by Su et al. [39]:

$$R = \frac{\varepsilon_1^i - \varepsilon_1^0}{\varepsilon_1^0} \tag{3}$$

Where: ε_1^i is the axial strain at the end of each dynamic disturbance cycle, and ε_1^0 is the axial strain at the corresponding starting point of the disturbance. The relative deformation coefficients of rock samples with different initial unloading damages under dynamic disturbance are shown in Fig. 10.

Based on Table 2 and Figs. 9 and 10, the following conclusions can be drawn:

(1) Under the action of dynamic disturbance and static load, the average strain rate of rock samples with different initial unloading damages shows a consistent trend during the constant velocity deformation stage, showing a non-linear pattern of smaller average strain rate under low initial unloading damage and significant increase in average strain rate under high initial unloading damage. The variation patterns of the two can also be well fitted by exponential functions. Compared with static load, under dynamic disturbance, the average axial strain rates under different initial unloading damages (70 %, 75 %, 80 %, 85 %, 90 %, and 95 %) increased by 4.22, 4.52, 5.26, 5.95, 9.45, and 20.53 × 10–7/s, respectively, with an increase of over 200 %; And at lower initial unloading damage (70–80 %), the difference in average strain rate between the two changes relatively little, with the difference only increasing by 1.00–1.07 times on the basis of 70 % initial unloading damage. However, at higher initial unloading damage (80–95 %), the difference in average axial strain rate between the two changes significantly, with the difference increasing by 1.25–4.86 times on the basis of 70 % initial unloading damage.

(2) The relative deformation coefficient time curve of rock samples with different initial unloading damages shows an S-shaped development trend during the dynamic disturbance stage. The axial deformation development can be divided into three stages: rapid small growth, low-speed stable growth, and high-speed large growth. As the initial unloading damage decreases, the S-shaped development trend of the relative deformation coefficient time curve becomes more evident. The overall slope of this curve increases with the rise in initial unloading damage. Concurrently, as the initial unloading damage increases, the relative deformation coefficient at the disturbance endpoint decreases. For instance, different initial unloading damages (70 %, 75 %, 80 %,

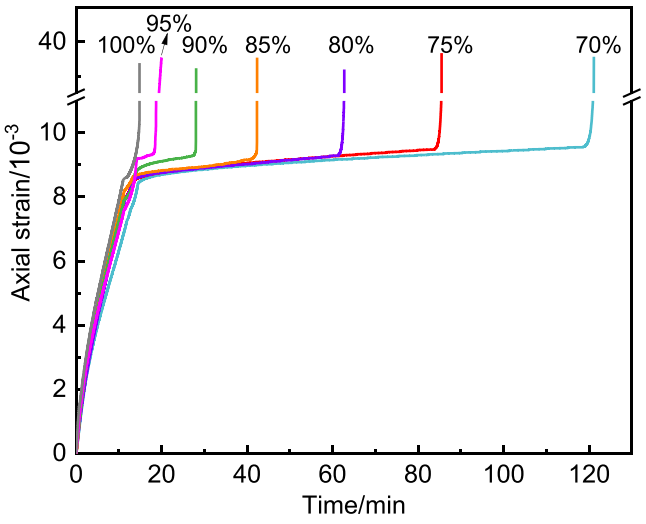

(a) Static load

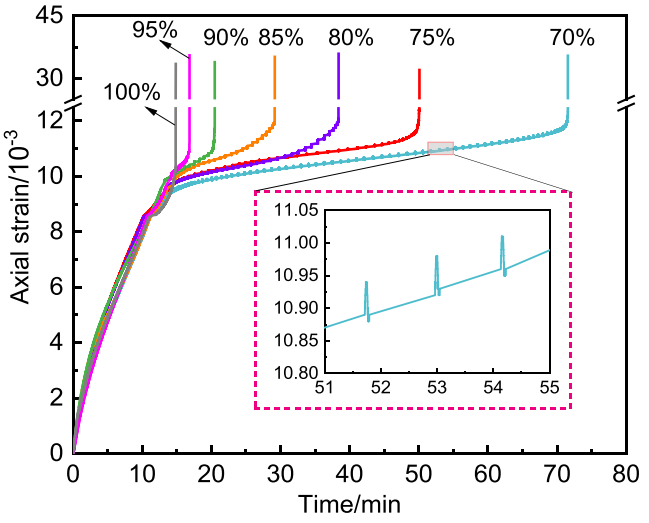

(b) Dynamic disturbance

Fig. 8. Axial strain-time curve.

Table 2
Corresponding load duration and strain increment results during the constant velocity deformation stage.

Initial unloading damage/%	Static load			Dynamic disturbance		
	Duration of load /min	Strain increment /10^{-3}	Average strain rate /(10^{-7}/s)	Duration of load /min	Strain increment /10^{-3}	Average strain rate /(10^{-7}/s)
70	95.93	0.69	1.20	45.88	1.49	5.41
75	64.30	0.56	1.45	27.03	0.97	5.98
80	42.26	0.42	1.66	17.85	0.74	6.91
85	22.78	0.37	2.71	9.84	0.51	8.64
90	10.77	0.24	3.71	4.43	0.35	13.17
95	3.35	0.15	7.46	1.31	0.22	27.99

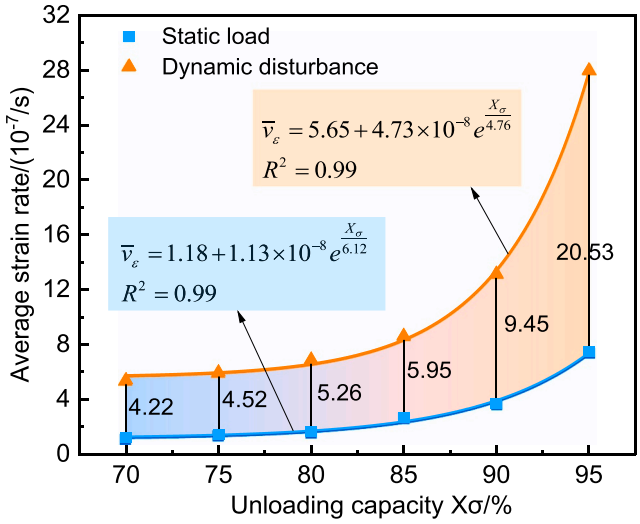

Fig. 9. Average strain rate-time curve under different initial unloading damages.

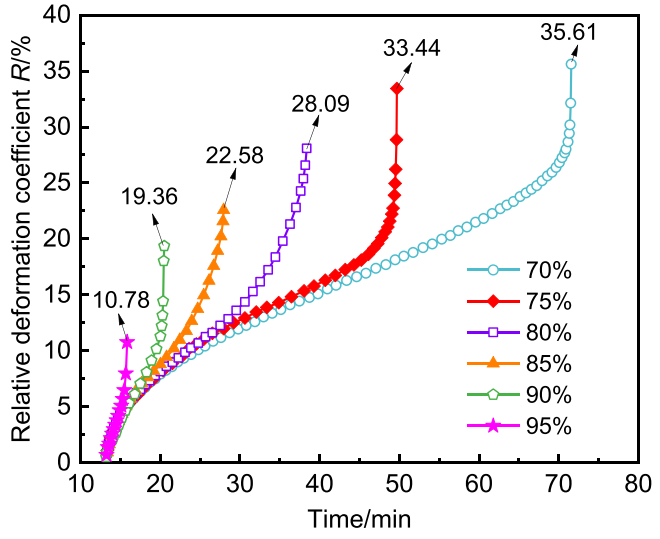

Fig. 10. Relative deformation coefficient-time curve under different initial unloading damages.

85 %, 90 %, and 95 %) correspond to relative deformation coefficients of 35.61 %, 33.44 %, 28.09 %, 22.58 %, 19.36 %, and 10.78 % at the disturbance endpoint. This indicates that higher initial unloading damage leads to a faster rate of irreversible damage deformation caused by dynamic disturbance. Conversely, lower initial unloading damage results in a slower irreversible damage deformation rate, but the cumulative irreversible deformation due to dynamic disturbances will be larger.

4. Mechanism of delayed unloading failure of sandstone under dynamic disturbance

The transition from stress to failure in rocks is a gradual process. Macroscopically, it involves the progression from stable fracture to unstable fracture, eventually leading to failure. Microscopically, it encompasses the emergence, development, convergence, and expansion of micro defects and newly formed cracks within the rock, ultimately forming macroscopic cracks of varying directions, scales, and quantities. Observing the development and evolution of internal cracks in rocks at the microscopic level is challenging in both laboratory and field settings. Therefore, particle flow numerical simulation software is employed to explore the delayed failure process of sandstone unloading under static loads and dynamic disturbances from the perspective of microscopic crack development and evolution.

4.1. Establishment of numerical models and parameter calibration

4.1.1. Establishment of numerical model

In the modeling process, the following aspects are primarily considered:

(1) The numerical model sample has a height of 100 mm and a diameter of 50 mm, meeting the requirement of a height-to-diameter ratio of 2.
(2) The rock used in the experiment is porous, calcium-cemented, sericite medium-grained quartz sandstone, with a particle size of approximately 0.3–0.5 mm [8]. However, considering computational power and efficiency, the minimum radius of the particles is selected as 0.8 mm. The ratio of the maximum particle radius to the minimum particle radius is 1.66, and it is uniformly distributed within the particle size range. This ensures that the particle number RES influence on the calculation results at the minimum scale of the model [45], that is $RES = (L/R_{\min})[1/(1 + R_{\max}/R_{\min})] > 10$. where L is the minimum size of the model, R_{min} is the minimum radius of the particles, and R_{max} is the maximum radius of the particles. Based on previous research [30,49], a parallel bonding contact model (LPBM) was employed to simulate rock samples, resulting in the sandstone model shown in Fig. 11.
(3) In triaxial test simulations, the flexible coupling particle method can be used to simulate actual flexible constraints [5,6,42]. The particle string connected by the linear contact bonding model (LCBM) is used for simulation. Since the contact bond does not transmit torque, the flexibility of the membrane is ensured, and the specified confining pressure conditions can be achieved by applying lateral force to the particle string. The flexible particle film adopts a hexagonal particle arrangement, and the radius of flexible film particles is set to 0.5 mm, which is 62.5 % of the minimum particle radius of rock, to prevent extrusion during the

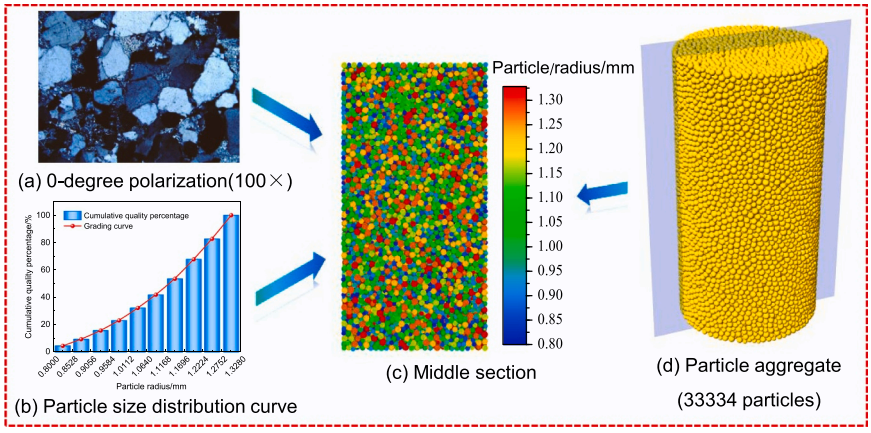

Fig. 11. Sandstone particle flow model.

deformation and failure process of rock particles. The upper and lower ends of the O-ring are used to fix the upper and lower ends of rock particles to limit lateral deformation. The final flexible triaxial loading model is shown in Fig. 12.

4.1.2. Microscopic parameter calibration

Since the simulated experiment is a triaxial unloading test, it requires the setting of two model parameters: the linear parallel bonding model (LPBM) [35,49] for rock particles and the linear contact bonding model (LCBM) [2,25] for the flexible particle film. The selection of microscopic parameters for these two contact models primarily considers the following:

(1) A trial-and-error method is used to conduct uniaxial compression simulations, which are then compared with indoor uniaxial compression tests to determine the microscopic parameters of the parallel bonding contact model.
(2) The trial-and-error method is again employed to conduct triaxial compression simulations. These are compared with the macroscopic test results of indoor triaxial compression tests under different confining pressures to determine the microscopic parameters of the linear contact bonding model.

According to the simulation approach described above, after multiple parameter adjustments, a more reasonable simulation result was obtained. The stress-strain curve of the uniaxial compression test is shown in Fig. 13, and the stress-strain curve of the numerical simulation

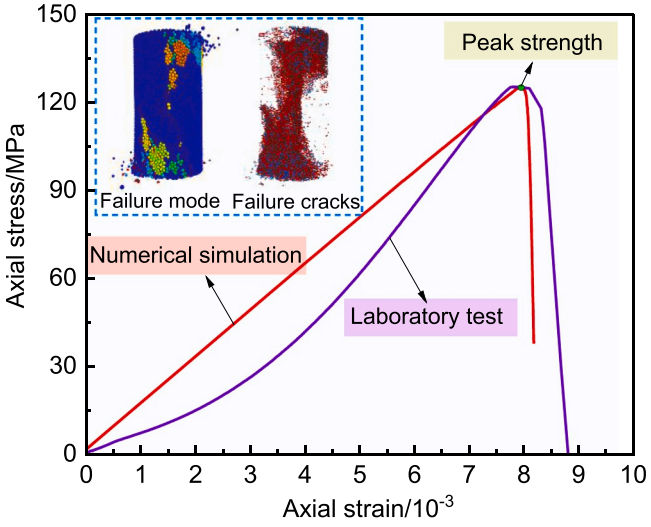

Fig. 13. Comparison of stress-strain curves in uniaxial compression test.

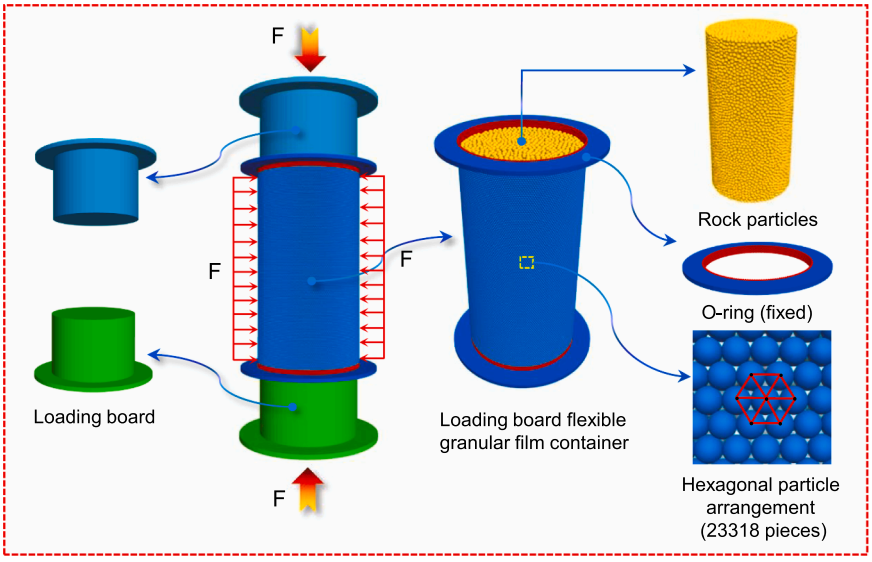

Fig. 12. Flexible three-axis loading model.

under different confining pressures is shown in Fig. 14. The final model parameters determined by trial calculations are listed in Table 3. The peak strength and strain obtained from the numerical simulation closely match the experimental results, with errors within 5 %, indicating that the microscopic parameters are reasonable.

4.2. Numerical simulation analysis of sandstone unloading delay failure under dynamic disturbance

4.2.1. Time delayed damage simulation analysis method

For time-delay failure tests, simply introducing a linear parallel bonding contact model is insufficient to achieve the expected results. Time effects must be incorporated into the model, and the stress corrosion model [36] (PSC) is particularly effective and widely used by many scholars.

The PSC model is primarily based on the linear parallel bonding contact model, which considers the corrosion rate V of its bonding diameter, and the stress corrosion reaction occurring at tensile defects. When the normal stress of the bonding bond reaches the contact cracking strength threshold, the parallel bond diameter D between the connecting particles gradually decreases, and the indirect contact normal stress of the bonding bond gradually increases. Based on this, a mechanism of rock time-dependent failure effect is established to simulate the damage evolution process of rocks over time, where the evolution equation of bond diameter D with time step t is shown in Eq. (4):

$$D = \begin{cases} D_0, & \sigma < \sigma_a \\ D_0 - \beta_1 e^{\beta_2(\sigma/\sigma_t)} t, & \sigma_a \le \sigma < \sigma_t \\ 0, & \sigma > \sigma_t \end{cases} \tag{4}$$

Where, σ is the normal stress of the bonding contact; σ_a is the threshold of the normal stress of the contact damage; σ_t is the tensile strength of the contact; β_1 and β_2 are material constants that depend on temperature and chemical environment, respectively; t is the time step. The corrosion process of the PSC model bonding diameter is shown in Fig. 15.

For the PSC model, there are three important parameters in the evolution equation of its bonding diameter D with time step t, namely β_1, β_2 and σ_a. Among them, β_1 and β_2 have an exponential relationship with the load duration t_f. That is, as β_1 and β_2 increase, the load duration t_f decays exponentially [19,40]. As for the σ_a parameter, as σ_a increases, t_f shows a trend of first increasing and then decreasing [28].

4.2.2. Analysis of time delay damage simulation results

The PSC model is introduced to simulate the unloading delay failure test under static load and dynamic disturbance, with model parameters repeatedly adjusted to obtain corresponding simulation results. The stress-strain curve and strain-time curve of the unloading delay failure test under static load and dynamic disturbance are shown in Figs. 16 and 17, respectively. The comparison of load duration for different initial unloading damage rock samples under static load and dynamic

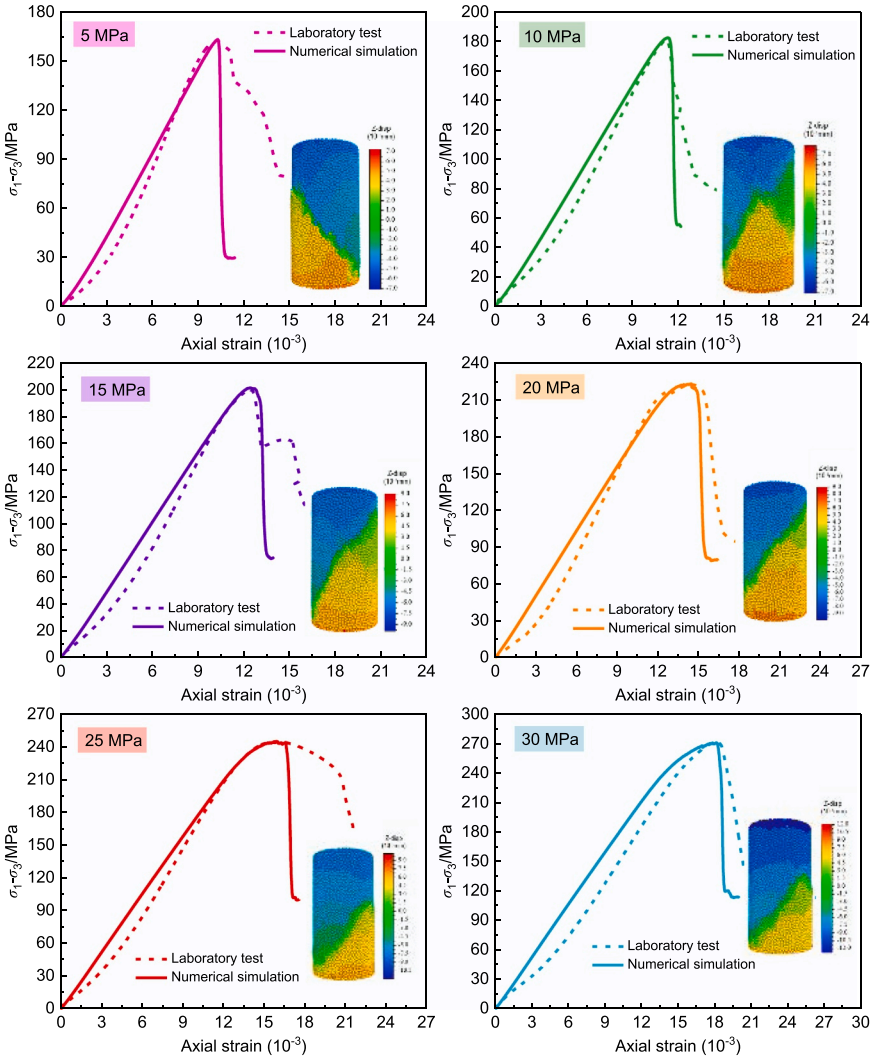

Fig. 14. Stress-strain curve under numerical simulation under different confining pressures.

Table 3
Microscopic parameter settings for contact model.

Parameter type	Microscopic parameters	Numerical value	Unit
Basic parameters of particles	Particle density ρ	2600	kg/m^3
	Porosity n	0.12	/
	Minimum radius of particles R_{min}	0.80	mm
	particle diameter ratio (R_{max}/R_{min})	1.66	/
	Damping β	0.7	/
	Sample height/ diameter	2.0	/
Linear parallel bonding model (LPBM) (Sandstone particles)	Effective modulus of linear elasticity E^*	7.0	GPa
	Linear elastic stiffness ratio k^*	2.0	/
	Effective modulus of bonding group $\overline{E}^*$	9.0	GPa
	Stiffness ratio of bonding group $\overline{k}^*$	2.0	/
	Tensile strength $\overline{\sigma}_c$	30.0	MPa
	Cohesion $\overline{c}$	25.0	MPa
	Internal friction angle $\overline{\phi}$	45.0	°
	Frictional coefficient μ	0.577	/
Linear contact bonding model (LCBM) (Flexible film particles)	Particle radius R	0.5	mm
	Particle density ρ	2000	kg/m^3
	Damping β	0.2	/
	Effective modulus E^*	50.0	MPa
	Stiffness ratio k^*	3.0	/
	Tensile resistance T_F	1.0×10^{300}	N
	Shear resistance S_F	1.0×10^{300}	N
	Interface spacing g_r	$0.01\times R$	mm

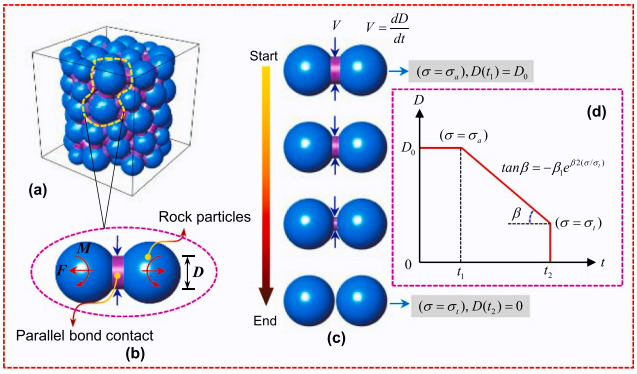

Fig. 15. Schematic diagram of PSC model.

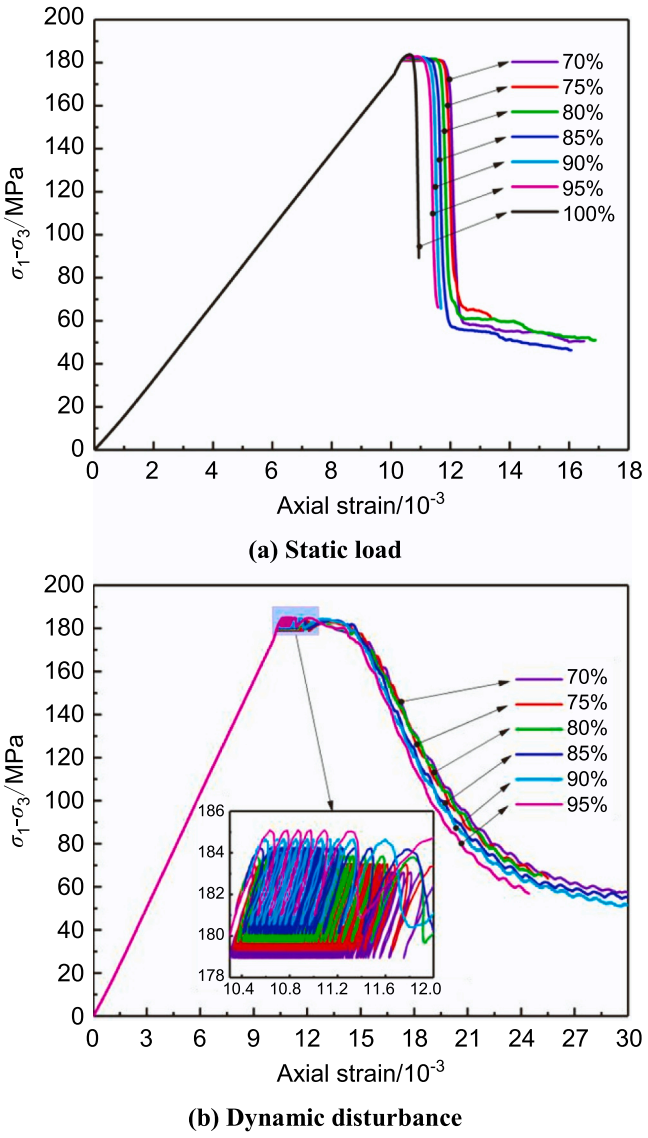

Fig. 16. Stress-strain curve.

disturbance is shown in Fig. 18.

From the analysis of Figs. 16–18, it is evident that the stress-strain curve of the numerical simulation experiment is consistent with the shape of the indoor test curve. Moreover, as initial unloading damage increases, the load duration exhibits a non-linear decay trend, consistent with the experimental results, with errors within 10 %. The numerical simulation results agree well with indoor experiments, confirming the reasonableness of the PSC model parameters (Table 4). Among them, φ_a in Table 4 is the lower limit value allowed for the reduction of bonding diameter, and $\varphi_a = D_{\min}/D_0$ is introduced to prevent the bonding diameter from decreasing to unrealistic values [36].

4.3. Analysis of delayed failure mechanism of sandstone unloading under dynamic disturbance

In numerical simulation experiments, the development of cracks directly reflects the failure mechanism. Therefore, monitoring and statistical analysis of the evolution of different crack numbers are crucial. Due to the inconvenience of analyzing the number of cracks at each time step in the simulation of each rock sample, three key time nodes are selected for analysis:

(1) The starting point of time-delay destruction is the start of the stress platform and the end of the initial unloading stage (initial unloading damage). This is used to analyze the number of cracks inside the rock sample after reaching the specified stress level.
(2) The endpoint of time-delay destruction: the end of the stress platform (critical failure point), indicating that after reaching the specified stress level, the rock sample must continue for a certain period to reach the critical failure point. This stage is used to analyze the development of cracks during the aging failure process.
(3) Residual strength point: the end of the experiment (complete failure point), primarily analyzing the development of cracks within a short period between the critical failure point and the complete failure point, to reflect the brittle failure characteristics of sandstone.

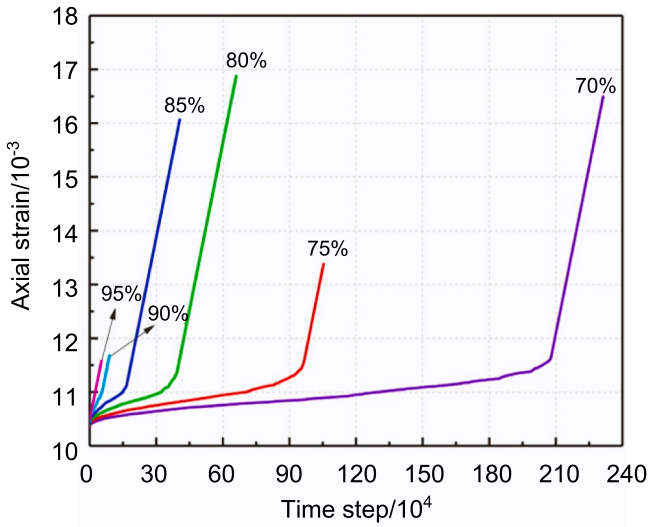

(a) Static load

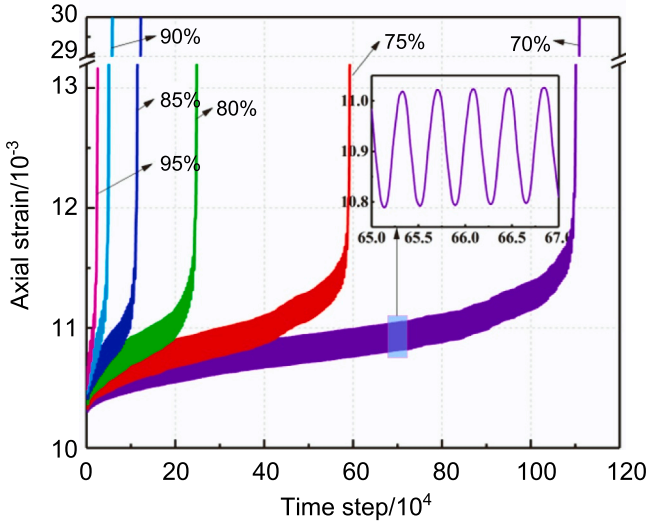

(b) Dynamic disturbance

Fig. 17. Axial strain-time curve.

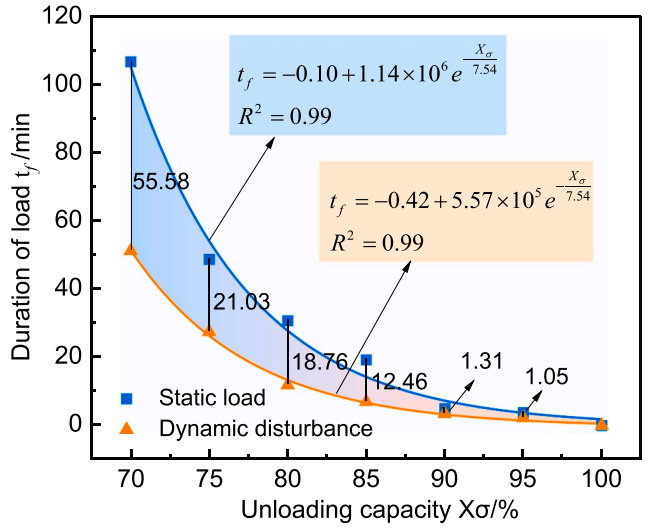

Fig. 18. Comparison of load duration under static load and dynamic disturbance (numerical simulation).

Table 4
PSC Model Microscopic Parameter Setting Table.

Parameter	β_1	β_2	σ_a	φ_a
Numerical value	1.60×10^{-8}	19.0	9.0 MPa	0.01

The curve of crack quantity at typical time nodes is shown in Figs. 19 and 20.

To quantitatively analyze the degree of damage and the proportion of tensile and shear cracks in each rock sample under static and dynamic disturbances, the fracture degree S is defined as the ratio of the total number of microcracks (N_0) during the delayed failure process to the total number of bonding contacts between particles before loading (N). The shear tensile crack ratio R is defined as the number of shear cracks (N_S) to he number of tensile cracks (N_T) during the delayed failure process. The specific definitions are given in Eqs. (5) and (6).

$$S = \frac{N_0}{N} \tag{5}$$

$$R = \frac{N_S}{N_T} \tag{6}$$

The comparison of crack numbers at different time nodes for

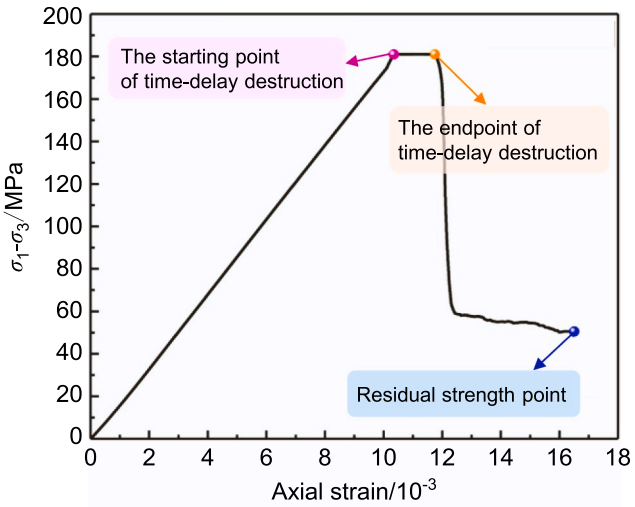

(a) Stress-strain curve

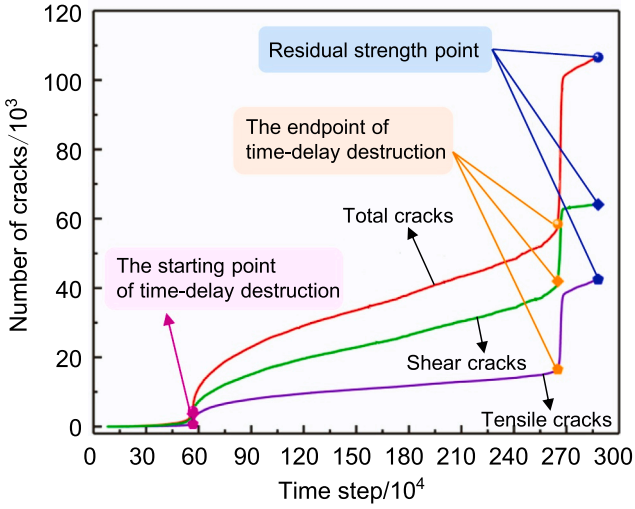

(b) Crack-time curve graph

Fig. 19. Numerical simulation test curve under typical static load (70 % initial unloading damage).

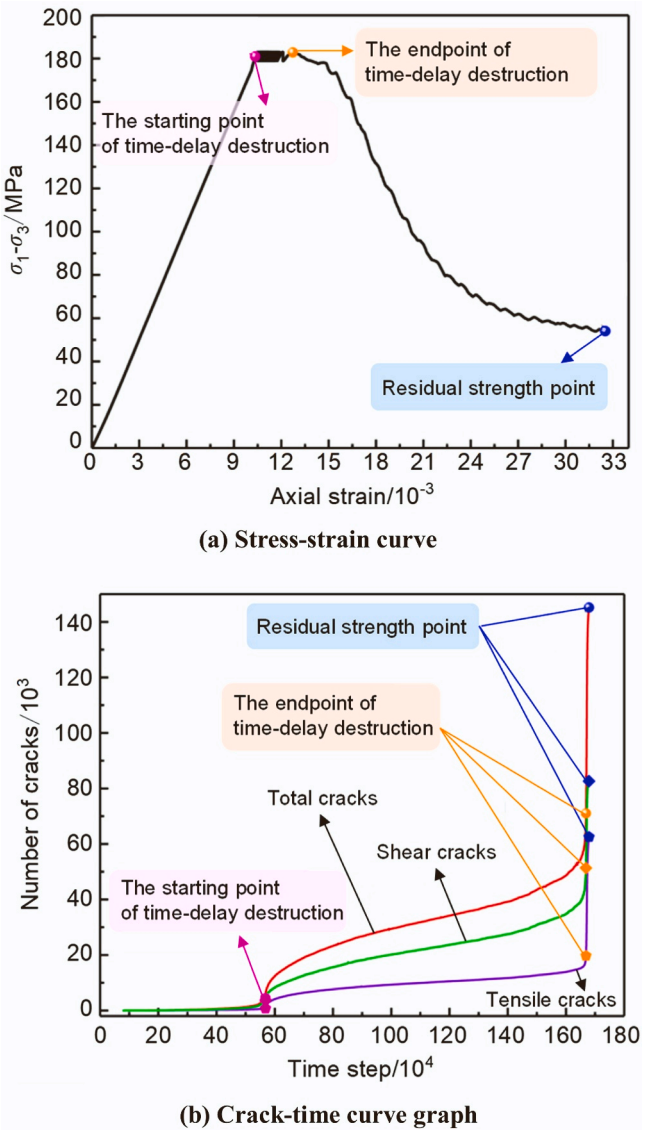

Fig. 20. Numerical simulation test curve under typical dynamic disturbance (70 % initial unloading damage).

different initial unloading damages under static loads and dynamic disturbances is shown in Fig. 21.

According to the analysis in Fig. 21, it can be concluded that:

(1) As shown in Fig. 21(a), at the onset of delayed failure, the number of cracks exhibits a nonlinear growth trend with increasing initial unloading damage. When the initial unloading damage increases from 70 % to 100 %, the total number of cracks, shear cracks, and tensile cracks increase by approximately 3.1, 3.2, and 2.5 times, respectively.

(2) As shown in Fig. 21(b), at the endpoint of delayed failure, the development pattern of crack numbers under static load and dynamic disturbance is generally consistent; that is, as initial unloading damage increases, the total number of cracks, shear cracks, and tensile cracks gradually decrease. When the stress level increases from 70 % to 100 %, the total number of cracks under static load and dynamic disturbance decreases from 58,473 and 710,461 to 13,925 and 13,925, respectively, reducing to 1/4 and 1/5, respectively. Compared to static loading, the total number of cracks with different initial unloading damages increased by approximately 2.8, 4.4, 3.1, 6.0, 4.9, and 3.4 times

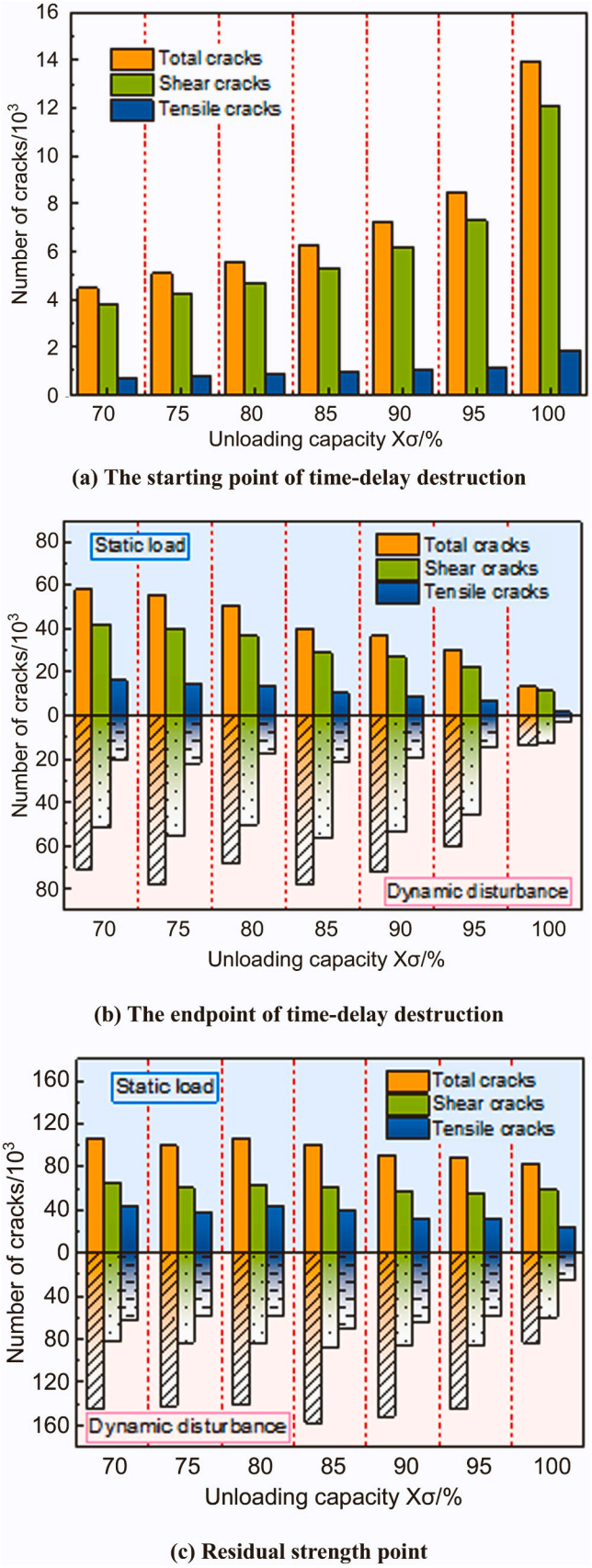

Fig. 21. Comparison of crack numbers under different initial unloading damages.

under dynamic disturbance during the delayed failure stage (from the starting point to the endpoint of delayed failure). These results indicate that under lower initial unloading damage, the degree of crack development within the rock sample is more severe. Additionally, dynamic disturbance exacerbates crack development within the rock sample, making it more prone to failure.

(3) As shown in Fig. 21(c), at the residual strength point, for the dynamic disturbance effect, the total number of cracks with different initial unloading damages increased by about 32.5–6.0 times compared to the starting point of time-delay destruction, and by about 16.6–5.0 times compared to the endpoint of time-delay destruction. Under static load, the above growth values were 23.9–6.0 times and 10.8–5.0 times, respectively. Compared to static loading, the total number of cracks with different initial unloading damages increased by about 5.8–3.3 times under dynamic disturbance between the time delayed failure endpoint and the residual strength point.

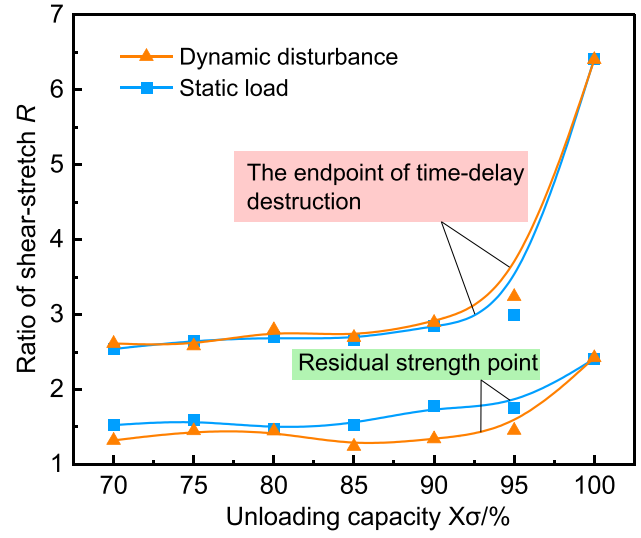

(a) Ratio of shear-stretch curve

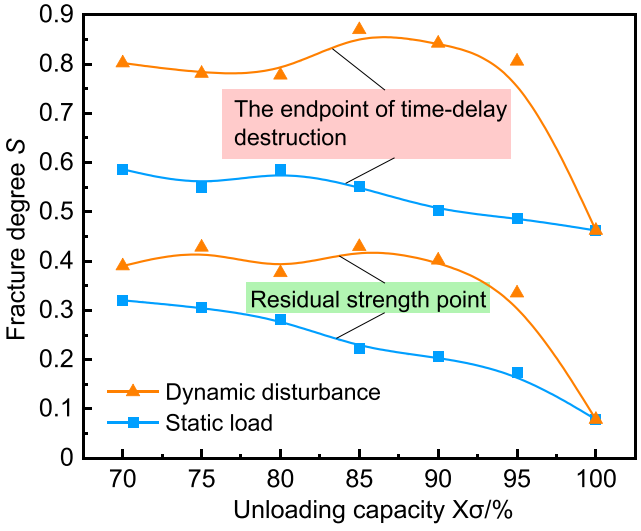

(b) Fracture degree

Fig. 22. Ratio of shear-stretch and Fracture degree curves under different initial unloading damages.

The comparison of shear tensile ratio and rupture degree under different initial unloading damages is shown in Fig. 22.

As shown in Fig. 22 (a):

(1) At the endpoint of time-delay failure, the ratio of shear-stretch under different initial unloading damages under dynamic disturbance and static load are generally consistent, both above 2.5, and both show a nonlinear growth trend with the increase of stress level. At the same time, when the initial unloading damage is below 90 %, the ratio of shear-stretch growth is slower, while when the initial unloading damage is above 90 %, the ratio of shear-stretch growth is faster. The results indicate that at the endpoint of time-delay failure, when the initial unloading damage is high, the shear to tensile ratio is large, mainly exhibiting shear characteristics. However, when the initial unloading damage is low, the shear to tensile ratio is small, and the tensile characteristics increase, resulting in a composite tensile shear characteristic.

(2) At the residual strength point, the shear-to-tensile ratio shows a slight increasing trend with increasing initial unloading damage. When the initial unloading damage increases from 70 % to 100 %, the shear-to-tensile ratio under static load and dynamic disturbance increases from 1.5 to 2.4 and 1.3–2.4, respectively. The shear-to-tensile ratio at the residual strength point is generally lower than that at the time-delay failure endpoint, with the ratio under static load being slightly higher than under dynamic disturbance. These results indicate that as the rock sample progresses from critical failure to complete failure, the internal shear-to-tensile ratio gradually decreases, and tensile characteristics are significantly enhanced. Moreover, dynamic disturbances, compared to static loads, lead to an increase in tensile failure characteristics.

As shown in Fig. 22 (b):

(1) At the endpoint of time-delay failure, the degree of rupture gradually decreases with increasing initial unloading damage. When the initial unloading damage increases from 70 % to 100 %, the degree of rupture under static load and dynamic disturbance decreases from 0.32 and 0.39–0.08 and 0.08, respectively. The rupture degree under different initial unloading damage levels is relatively low, overall below 0.40, but the rupture degree under dynamic disturbance is higher than that under static load.

(2) At the residual strength point, the degree of rupture under different initial unloading damage levels is relatively high, overall above 0.45. Under dynamic disturbance, the degree of rupture at different initial unloading damage levels increased by 0.41, 0.35, 0.40, 0.44, 0.44, 0.47, and 0.38, respectively, compared to the time-delay failure endpoint. Moreover, compared to static loads, the degree of rupture under dynamic disturbances is 0.19–0.34 higher. These results indicate that high initial unloading damage corresponds to a decreased degree of rupture in the rock sample, while lower initial unloading damage leads to an increased degree of rupture, resulting in more severe internal damage and fragmentation. Dynamic disturbances further exacerbate the internal damage and fragmentation of the rock sample, leading to greater overall fragmentation.

5. Conclusion

(1) The load duration of the triaxial unloading delay failure test exhibits an exponential decay trend with increasing initial unloading damage. Compared to static load effects, the load duration under dynamic disturbance decreases by more than 43 %, and the average axial strain rate increases by over 200 %.

(2) The total number of cracks at the onset of triaxial unloading delay failure is relatively small, but it significantly increases by the endpoint of delay failure. As the initial unloading damage decreases, the total number of cracks rises markedly, leading to more severe rock sample fracture. Furthermore, under dynamic disturbance, the total number of cracks for different initial unloading damages also increases significantly compared to static loads. The shear-to-tensile ratio at the endpoint of triaxial unloading delay failure shows a nonlinear growth trend with increasing initial unloading damage, and the overall shear-to-tensile ratio exceeds 2.5. Under dynamic disturbance, the shear-to-tensile ratio at the endpoint of triaxial unloading delay failure with different initial unloading damages is essentially equivalent to that under static load.

CRediT authorship contribution statement

Pengfei Xu: Visualization, Software. **Jianlin Li:** Methodology, Funding acquisition. **Mingyang Wang:** Formal analysis, Conceptualization. **Huafeng Deng:** Writing – review & editing, Writing – original draft, Funding acquisition, Conceptualization. **Yening Huang:** Writing – original draft, Investigation, Data curation. **Yao Xiao:** Software, Data curation.

Declaration of Competing Interest

The authors declare that they have no known competing financial interests or personal relationships that could have appeared to influence the work reported in this paper.

Acknowledgements

The authors gratefully acknowledge the financial support provided by the National Natural Science Foundation of China (Grant No. U22A20600, U2034203).

References

[1] M. Askaripour, A. Saeidi, A. Rouleau, P. Mercier-Langevin, Rockburst in underground excavations: a review of mechanism, classification, and prediction methods, Undergr. Space 7 (4) (2022) 577–607.
[2] N. Bahrani, P.K. Kaiser, Estimation of confined peak strength of crack-damaged rocks, Rock. Mech. Rock. Eng. 50 (2017) 309–326.
[3] M.K.P.K. Cai, P.K. Kaiser, Y. Tasaka, T. Maejima, H. Morioka, M. Minami, Generalized crack initiation and crack damage stress thresholds of brittle rock masses near underground excavations, Int. J. Rock. Mech. Min. Sci. 41 (5) (2004) 833–847.
[4] B.R. Chen, X.T. Feng, H.J. Ming, H. Zhou, X.H. Zeng, G.L. Feng, Y.X. Xiao, Evolution law and mechanism of rockburst in deep tunnel: time delayed rockburst. Chin. J. Rock. Mech. Eng. 31 (3) (2012) 561–569 (in Chinese).
[5] G. Cheung, C. O'Sullivan, Effective simulation of flexible lateral boundaries in two- and three-dimensional DEM simulations, Particuology 6 (6) (2008) 483–500.
[6] M.B. Cil, K.A. Alshibli, 3D analysis of kinematic behavior of granular materials in triaxial testing using DEM with flexible membrane boundary, Acta Geotech. 9 (2014) 287–298.
[7] H.F. Deng, J.L. Li, C.J. Deng, L.H. Wang, T. Lu, Analysis of sampling in rock mechanics test and compressive strength prediction methods, Rock. Soil Mech. 32 (11) (2011) 3399–3403.
[8] H.F. Deng, Y.Y. Hu, J.L. Li, Z.Y. Xiao, M.L. Zhou, Yu Hu, Experimental research on load/unload response ratio considering hysteresis effect of rock, Chin. J. Rock. Mech. Eng. 34 (Supplement 1) (2015) 2915–2921 (in Chinese).
[9] H.F. Deng, Z. Wang, J.L. Li, Y. Hu, X.J. Zhang, Compressive strength correction method of flaw sample in rock mechanics test, Chin. J. Undergr. Space Eng. 13 (2) (2017) 307–313 (in Chinese).
[10] H.F. Deng, Z. Wang, J.L. Li, Q. Jiang, H.B. Zhang, Effect of unloading rate and pore water pressure on mechanical properties of sandstone, Chin. J. Geotech. Eng. 39 (11) (2017) 1976–1983 (in Chinese).
[11] K. Du, X.B. Li, L.J. Dong, M. Tao, J. Zhou, Fracture mechanism of rock induced by true-triaxial unloading and heterology dynamic disturbance, Chin. J. Rock. Mech. Eng. 34 (S2) (2015) 4047–4053 (in Chinese).
[12] C. Fan, X.T. Feng, L. Fu, J. Zhao, C. Yang, Z. Yao, F. Wei, Evolution law and mechanism of time-delayed spalling in a deep TBM tunnel: a case study, Eng. Geol. 325 (2023) 107309.
[13] X.T. Feng, B.R. Chen, H.J. Ming, S.Y. Wu, Y.X. Xiao, G.L. Feng, H. Zhou, S.L. Qiu, Evolution law and mechanism of rockbursts in deep tunnels: immediate rockburst, Chin. J. Rock. Mech. Eng. 31 (3) (2012) 433–444 (in Chinese).
[14] X.T. Feng, Y. Yu, G.L. Feng, Y.X. Xiao, B.R. Chen, Q. Jiang, Fractal behaviour of the microseismic energy associated with immediate rockbursts in deep, hard rock tunnels, Tunn. Undergr. Space Technol. 51 (2016) 98–107.
[15] X.T. Feng, Y.X. Xiao, G.L. Feng, Z.B. Yao, B.R. Chen, C.X. Yang, G.S. Su, Study on the development process of rockbursts, Chin. J. Rock. Mech. Eng. 38 (4) (2019) 649–673 (in Chinese).
[16] Q. Gu, Q. Zhang, S. Ye, T. Li, W. Dai, Experimental investigation on the shear mechanical behavior and energy evolution of sandstone subjected to pre-peak cyclic loading, Soil Dyn. Earthq. Eng. 177 (2024) 108374.
[17] M.C. He, D.Q. Liu, W.L. Gong, C.C. Wang, J. Kong, S. Du, S. Zhang, Development of a testing system for impact rockbursts, Chin. J. Rock. Mech. Eng. 33 (09) (2014) 1729–1739 (in Chinese).
[18] M.C. He, F.Q. Ren, D.Q. Liu, S.D. Zhang, Experimental study on strain burst characteristics of sandstone under true triaxial loading and double faces unloading in one direction, Rock. Mech. Rock. Eng. 54 (2021) 149–171.
[19] G.H. Hu, T. Xu, C.F. Chen, X.K. Yang, A microscopic study of creep and fracturing of brittle rocks based on discrete element method, Eng. Mech. 35 (9) (2018) 36–46 (in Chinese).
[20] L. Hu, X.T. Feng, Z.B. Yao, W. Zhang, W.J. Niu, X. Bi, Y.X. Xiao, Rockburst time warning method with blasting cycle as the unit based on microseismic information time series: a case study, Bull. Eng. Geol. Environ. 82 (4) (2023) 121.
[21] J. Hu, M. He, H. Li, Z. Tao, D. Liu, T. Cheng, D. Peng, Rockburst hazard control using the excavation compensation method (ECM): a case study in the Qinling Water Conveyance Tunnel, Engineering 34 (2024) 154–163.
[22] R.Q. Huang, D. Huang, Experimental research on affection laws of unloading rates on mechanical properties of Jinping marble under high geostress, Chin. J. Rock. Mech. Eng. 29 (1) (2010) 21–33 (in Chinese).
[23] Y.H. Huang, S.Y. Wu, C. Yang, Experimental study on the failure behaviors of sandstone specimens with two fissures under triaxial loading and unloading conditions, Eng. Fract. Mech. 298 (2024) 109933.
[24] Q. Jiang, X.T. Feng, T.B. Xiang, G.S. Su, Rockburst characteristics and numerical simulation based on a new energy index: a case study of a tunnel at 2,500 m depth, Bull. Eng. Geol. Environ. 69 (2010) 381–388.
[25] C.Y. Kwok, M.D. Bolton, DEM simulations of thermally activated creep in soils, Géotechnique 60 (6) (2010) 425–433.
[26] Z. Li, J.M. Wang, Geological characters of rockburst in lujialing tunnel and its prevention methods, Chin. J. Rock. Mech. Eng. 24 (18) (2005) 3398–3402 (in Chinese).
[27] X.B. Li, F.Q. Gong, S.F. Wang, D.Y. Li, M. Tao, J. Zhou, L.Q. Huang, C.D. Ma, K. Du, F. Feng, Coupled static-dynamic loading mechanical mechanism and dynamic criterion of rockburst in deep hard rock mines, Chin. J. Rock. Mech. Eng. 38 (04) (2019) 708–723 (in Chinese).
[28] H. Li, N.T. William, J. Daemen, J. Zhou, C.K. Ma, A power function model for simulating creep mechanical properties of salt rock, J. Cent. South Univ. 27 (2) (2020) 578–591.
[29] H. Li, S.Q. Yang, Z. Yang, X.P. Zhou, W.L. Tian, S.S. Wang, Experimental and numerical study on the mechanical behaviors and crack propagation of sandstone containing two parallel fissures, Theor. Appl. Fract. Mech. 126 (2023) 103965.
[30] X.Z. Li, X.P. Xiao, K. Xie, H.F. Yang, L. Xu, T.F. Li, A generalizable parameter calibration framework for discrete element method and application in the compaction of red-bed soft rocks, Constr. Build. Mater. 444 (2024) 137734.
[31] G.M. Lu, Y.H. Li, X.W. Zhang, J.P. Liu, Fatigue deformation characteristics of yellow sandstone under cyclic loading, Chin. J. Geotech. Eng. 37 (10) (2015) 1886–1892 (in Chinese).
[32] Z.H. Kang, Z.X. Gao, X.D. Ding, Y.X. Wang, Disturbance response criterion based rockburst analysis, J. Hohai Univ. (Nat. Sci. Ed.) 31 (2) (2003) 188–192 (in Chinese).
[33] C.D. Ma, X.B. Li, F. Chen, J.C. Xu, Experimental study on the influence of uniaxial dynamic and static combined loading on the mechanical properties of rocks, Min. Res. Dev. 24 (4) (2004) 1–4 (in Chinese).
[34] Ministry of Water Resources of the People's Republic of China, SL264-2001 Rock Test Regulations for Water Conservancy and Hydropower Engineering, China Water Resources and Hydropower Press, Beijing, 2001 (in Chinese).
[35] D.O. Potyondy, P.A. Cundall, A bonded-particle model for rock, Int. J. Rock. Mech. Min. Sci. 41 (8) (2004) 1329–1364.
[36] D.O. Potyondy, Simulating stress corrosion with a bonded-particle model for rock, Int. J. Rock. Mech. Min. Sci. 44 (5) (2007) 677–691.
[37] Q.H. Qian, Definition, mechanism, classification and quantitative forecast model of rockburst and pressure bump, Rock. Soil Mech. 35 (1) (2014) 1–6 (in Chinese).
[38] S.L. Qiu, X.T. Feng, C.Q. Zhang, J.B. Yang, Experimental research on mechanical properties of deep marble under different initial damage levels and unloading paths, Chin. J. Rock. Mech. Eng. 31 (08) (2012) 1686–1697 (in Chinese).
[39] G.S. Su, L.H. Hu, X.T. Feng, J.H. Wang, X.H. Zhang, True triaxial experimental study of rockburst process under low frequency cyclic disturbance load combined with static load, Chin. J. Rock. Mech. Eng. 35 (07) (2016) 1309–1322 (in Chinese).
[40] J.S. Sun, M. Chen, Q.H. Jiang, W.B. Lu, C.B. Zhou, Numerical simulation of mesomechanical characteristics of creep demage evolution for Jingping marble, Rock. Soil Mech. 34 (12) (2013) 3601–3608 (in Chinese).
[41] X.N. Wang, R.Q. Huang, Analysis of the influence of the dynamic disturbance on rock burst, Mt. Res. 16 (3) (1998) 188–192 (in Chinese).
[42] Y.H. Wang, S.C. Leung, Characterization of cemented sand by experimental and numerical investigations, J. Geotech. Geoenviron. Eng. 134 (7) (2008) 992–1004.

[43] C. Wang, L.Z. Tang, L.P. Cheng, Y. Chen, T. Liu, Y.H. Wei, Dynamic characteristics of skarn subjected to frequent dynamic disturbance under combined action of high axial compression and confining pressure, Rock. Soil Mech. 39 (12) (2018) 4537–4546 (in Chinese).
[44] F. Wang, P. Cao, Y. Wang, R. Hao, J. Meng, J. Shang, Combined effects of cyclic load and temperature fluctuation on the mechanical behavior of porous sandstones, Eng. Geol. 266 (2020) 105466.
[45] X.Y. Wang, S.L. Huang, X.L. Ding, H.M. Zhou, Study on the effect of inhomogeneous bedding plane on the mechanical properties of uniaxial compression of layered rock mass, Rock. Soil Mech. 42 (02) (2021) 581–592 (in Chinese).
[46] X.J. Wei, T.T. Chen, X. Wang, X.F. Yu, L.Y. Zhou, Research and progress on rock burst hazards, Mod. Tunn. Technol. 57 (2) (2020) 1–12 (in Chinese).
[47] J.Q. Xiao, D.X. Ding, F.L. Jiang, G. Xu, Fatigue damage variable and evolution of rock subjected to cyclic loading, Int. J. Rock. Mech. Min. Sci. 47 (3) (2010) 461–468.
[48] P.F. Xu, H.F. Deng, H.B. Zhang, M. Peng, G.Y. Li, Q. Jiang, X.Z. Chen, Time-lag uniaxial compression failure characteristics of sandstone under different stress levels, Rock. Soil Mech. 42 (11) (2021) 3041–3050+3078 (in Chinese).
[49] Z. Xu, Z. Wang, W. Wang, P. Lin, J. Wu, An integrated parameter calibration method and sensitivity analysis of microparameters on mechanical behavior of transversely isotropic rocks, Comput. Geotech. 142 (2022) 104573.
[50] Z.Y. Ye, X.B. Li, Z.L. Zhou, T.B. Yin, X.L. Liu, Static-dynamic coupling strength and deformation characteristics of rock under triaxial compression, Rock. Soil Mech. 30 (07) (2009) 1981–1986 (in Chinese).
[51] S. Zhang, T. Ma, C.A. Tang, P. Jia, Y. Wang, Microseismic monitoring and experimental study on mechanism of delayed rockburst in deep-buried tunnels, Rock. Mech. Rock. Eng. 53 (2020) 2771–2788.
[52] H. Zhang, Q. Sun, J. Geng, H. Jia, Effect of high temperature on physical properties of yellow sandstone, Heat. Mass Transf. 57 (12) (2021) 1981–1995.
[53] K. Zhao, Y. Liu, D. Yang, B. Li, Z. Huang, C. Huang, X. Lan, Fatigue mechanical properties and Kaiser effect characteristics of the saturated weakly cemented sandstone under different loading rate conditions, Eng. Geol. (2024) 107732.
[54] D.P. Zhou, K.R. Hong, Characteristics and prevention measures of rock burst in taipingyi tunnel, Chin. J. Rock. Mech. Eng. 14 (2) (1995) 171–178 (in Chinese).
[55] J. Zhou, Y. Zhang, C. Li, H. He, X. Li, Rockburst prediction and prevention in underground space excavation, Undergr. Space 14 (2024) 70–98.

Deng Huafeng, male, born in 1979, doctoral supervisor, currently a professor. Mainly engaged in research work in geotechnical engineering.